JOURNAL OF GUIDANCE, CONTROL, AND DYNAMICS
Vol. 24, No. 2, March–April 2001

Synchronized Rotation of Multiple Autonomous Spacecraft with Rule-Based Controls: Experimental Study

P. K. C. Wang* and J. Yee†
University of California, Los Angeles, California 90095-1594
and
F. Y. Hadaegh‡
Jet Propulsion Laboratory, California Institute of Technology, Pasadena, California 91109-8099

An experimental study is made on the synchronized continuous-rotation of multiple air-levitated autonomous model spacecraft about a fixed axis by means of simple rule-based controls. These controls differ from the conventional ones, which require processing of numerical sensor data. The controls depend solely on the occurrence and timing of certain discrete event sequences. Thus, the controlled model spacecraft is a hybrid continuous-time and discrete-event system. Experimental results show that the proposed rule-based controls are effective in achieving rotational motion with synchronized angular velocity and phase. A description of the experimental setup and a brief discussion of the design of the air-levitated model spacecraft is given. Then, the details on the development of rule-based controls and the derivation of a dynamic model for the resulting hybrid system are presented followed by the presentation and interpretation of the experimental results.

I. Introduction

RECENT interest in formation flying of multiple autonomous spacecraft led to a number of studies in the coordination and control of multiple spacecraft.[1–5] A particular mode of operation is to rotate the spacecraft synchronously about a given axis.[6] This mode is useful in the continuous observation of a planetary surface using cameras attached to a number of spacecraft. To simulate the space environment in the laboratory, it is necessary to levitate the model spacecraft. In this paper, we present the results of an experimental study of synchronized rotation of multiple autonomous spacecraft simulated by air-levitated spheres equipped with lasers, optical sensors, infrared transceivers, and motor–flywheel systems for control. The main objective is to demonstrate that synchronized rotation can be achieved by using simple rule-based controls activated only by the occurrence and timing of certain sequences of discrete events.

The use of large air-levitated multiarm mobile robots for performing certain tasks such as target rendezvous and capture has been studied earlier.[7,8] In these works, the controls are generated by numerical data from sensors. Recently, the formation alignment of multiple air-levitated minivehicles with rule-based controls activated by discrete events has been studied experimentally.[9] This approach of this study is in the same spirit as that of Ref. 9. The objective here is to rotate continuously a number of air-levitated model spacecraft about a fixed axis in a synchronized manner. The paper begins with a description of the experimental setup. Then the design of air-levitated model spacecraft is discussed briefly. This is followed by a detailed discussion of the rule-based controls and the derivation of a dynamic model for the resulting hybrid system. The paper concludes with the presentation and interpretation of the experimental results.

II. Experimental Setup: Model Spacecraft Design

This experiment involves multiple autonomous spacecraft simulated by air-levitated spheres, one of which serves as the reference spacecraft for the remaining spacecraft. Hereafter, the reference spacecraft will be referred to as the leader and the remaining spacecraft as followers. At the beginning of an experiment, the leader rotates about its vertical body axis with certain angular velocity ω_d. It is required that each follower rotates continuously about its vertical body axis in synchrony with the leader's rotational motion.

The model spacecraft is composed of two hemispherical aluminum shells. The bottom shell has a platform on which a dc motor and a microcontroller are mounted. The rotational motion of the sphere is produced by the reaction torque of a dc motor, with its stator rigidly attached to the bottom hemisphere and its rotor attached to a stainless steel flywheel as shown in Fig. 1.

A. Levitation System

Here, each model spacecraft is levitated by a spherical air bearing driven by a single air inlet orifice at the bearing center. The external pressurized air source is connected to the orifice through a cavity for smoothing the airflow in the presence of possible source pressure fluctuations (Fig. 2). The cavity also helps to prevent possible model spacecraft damage due to sudden loss of air pressure. First, the equilibrium height h of the model spacecraft above the lower spherical bearing surface as a function of the air supply pressure p_s is determined so that a suitable operating point for levitation can be selected. The analytical details are given in Appendix A. Using the values of the parameters for our experimental setup given in Table 1B of Appendix B, the computed equilibrium height is $h = 3.408 \times 10^{-4}$ in.

B. Motor–Flywheel System

The motion of the sphere is produced by the reaction torque of the motor, whose stator is rigidly attached to the sphere. The rotor of the motor is attached to a flywheel. To analyze the dynamic behavior of the motor–flywheel system, let θ_1 and θ_2 denote the rotation angles of the motor stator and the flywheel, respectively, relative to an inertial frame (Fig. 1). The equations of motion for θ_1 and θ_2 are given by

$$I_1\ddot{\theta}_1 + \nu(\dot{\theta}_1 - \dot{\theta}_2) = -\tau(t) \tag{1a}$$

$$I_2\ddot{\theta}_2 + \nu(\dot{\theta}_2 - \dot{\theta}_1) = \tau(t) \tag{1b}$$

where $\dot{\theta}_i = \mathrm{d}\theta_i/\mathrm{d}t$ and $\ddot{\theta}_i = \mathrm{d}^2\theta_i/\mathrm{d}t^2$, I_1 and I_2 are the moments of inertia of the motor stator plus the sphere and the rotor–flywheel system about the vertical axis, respectively, ν is the coefficient of friction between the motor rotor and stator, and τ is the torque. We have neglected the viscous drag due to the air film between the sphere and the base and also between the sphere and the surrounding air. Evidently, the motor and the flywheel are coupled only by friction.

Received 11 June 1999; revision received 1 September 2000; accepted for publication 11 November 2000.

*Professor, Department of Electrical Engineering. Member AIAA.
†Graduate Student, Department of Electrical Engineering.
‡Senior Research Scientist and Technical Supervisor, Guidance and Control Analysis. Associate Fellow AIAA.

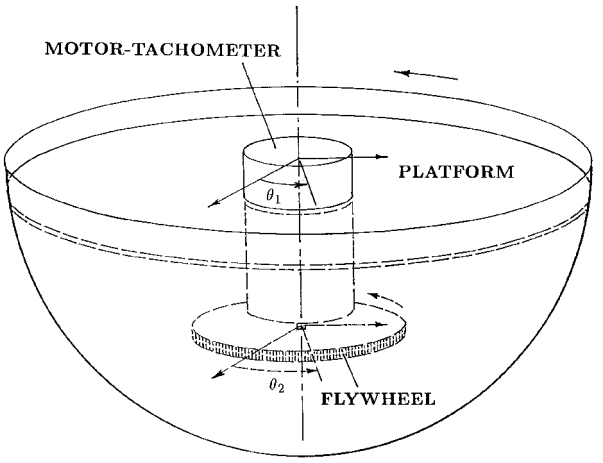

Fig. 1 Bottom hemisphere of model spacecraft.

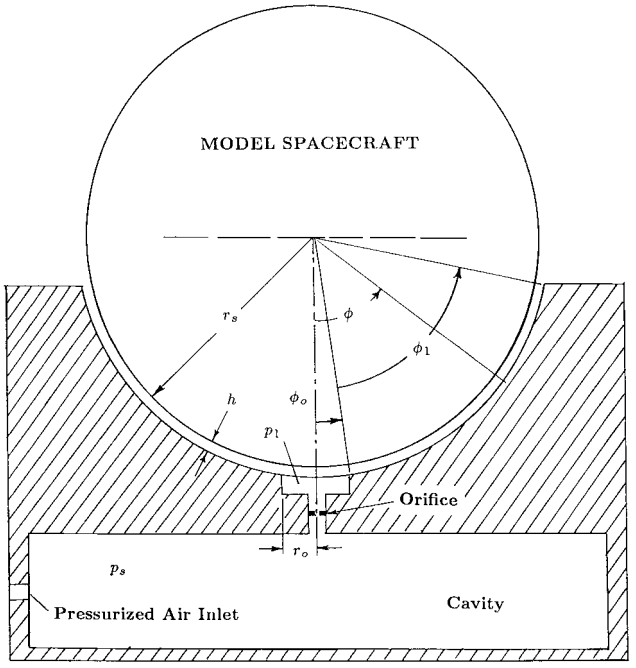

Fig. 2 Section of the air bearing for model spacecraft.

From Eq. (1), it can be readily deduced that θ_1 satisfies the following equation:

$$I_1\ddot{\theta}_1 + \nu[1 + (I_1/I_2)]\dot{\theta}_1 = -\tau(t) \tag{2}$$

For a step input torque $\tau(t) = \tau_0$, $t > 0$, the steady-state value for the angular velocity $\dot{\theta}_1$ is

$$\dot{\theta}_{1ss} = -[I_2/(I_1 + I_2)]\tau_0/\nu \tag{3}$$

Evidently, $\dot{\theta}_{1ss}$ is inversely proportional to the friction coefficient ν, which is not precisely known. To eliminate this undesirable feature, we introduce a linear velocity feedback control of the form

$$\tau(t) = -K[\hat{\omega}_d(t) + \dot{\theta}_2(t) - \dot{\theta}_1(t)] \tag{4}$$

where K is a positive constant feedback gain and $\hat{\omega}_d(t)$ is a given desired angular velocity at time t. Substituting Eq. (4) into Eq. (2) and making use of Eq. (1) to eliminate $\dot{\theta}_2$ lead to the following equation for θ_1:

$$[I_1/(\nu + K)]\ddot{\theta}_1 + [1 + (I_1/I_2)]\dot{\theta}_1 = K\hat{\omega}_d/(\nu + K) \tag{5}$$

Now, the steady-state value for $\dot{\theta}_1$ corresponding to a given constant $\hat{\omega}_d$ is given by

$$\dot{\theta}_{1ss} = [I_2/(I_1 + I_2)]K\hat{\omega}_d/(\nu + K) \tag{6}$$

If we choose $K \gg \nu$, then

$$\dot{\theta}_{1ss} \approx [I_2/(I_1 + I_2)]\hat{\omega}_d \tag{7}$$

Thus, $\dot{\theta}_{1ss}$ is insensitive to the value of ν. The size of the flywheel is chosen so that the maximum value of $\dot{\theta}_{1ss}$ is less than 0.3 revolutions per second.

To implement feedback control (4), the relative angular velocity $\dot{\theta}_2 - \dot{\theta}_1$ is measured by means of a tachometer attached directly to the rotor of the motor. In our actual motor–flywheel system, the tachometer output, after signal conditioning, provides a voltage proportional to the angular speed , which is controlled by an on-the-fly pulse-width modulation (PWM) scheme. That is, rather than feeding set binary words corresponding to set power levels into the motor control as in the usual approach, the microcontroller looks at the tachometer output every millisecond and compares it with the desired value $\hat{\omega}_d$. If the tachometer reading is higher than $\hat{\omega}_d$, the motor is deprived of power for the next millisecond. On the other hand, if the tachometer reading is lower than $\hat{\omega}_d$, full power is applied to the motor for the next millisecond. We found that this scheme gave us smoother motor operation and more operating power levels than other PWM schemes. Thus, the motor's angular velocity is controlled directly by specifying $\hat{\omega}_d$, whose desired value is determined by a rule-based control algorithm to be described later.

C. Sensor and Communication Systems

To determine the relative rotational motion of the model spacecraft, each sphere is equipped with a laser mounted inside the top spherical shell. The laser sends out a beam through a 45-deg prism attached to a platform with an adjustable tilt angle. The beam is intercepted by a sensor mounted on the top hemisphere. The sensor is composed of four 0.5 × 2 cm solar cells covering all viewing directions. When any cell is activated by the laser beam, a binary output is produced by the sensor unit.

The communication between the model spacecraft is provided by an infrared (IR) transceiver inside each sphere. The transceiver also serves as a telemetry device for model spacecraft data. All of the electronic devices and the motor are powered by two 9-V lithium batteries. Figure 3 gives an exposed view of the model spacecraft showing the sensor, the IR transceiver, the miniboard (designed by F. Martin of the Massachusetts Institute of Technology) using the

Fig. 3 Photograph of the interior of the model spacecraft showing the miniboard micro-controller, sensor unit, batteries, and the interface electronics.

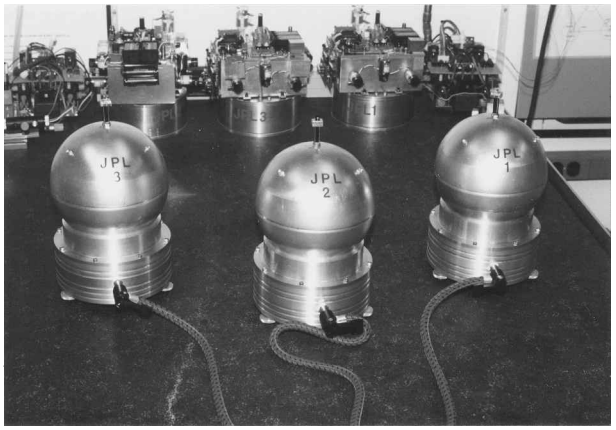

Fig. 4 Photograph of the experimental setup.

Motorola 68HC11 microcontroller, and the interface electronics. A photograph of the experimental setup consisting of air-levitated model spacecraft is given in Fig. 4. The model spacecraft were carefully balanced so that their rotational axes coincide with the vertical axes of their sensors. The tilt angle of the prism for the laser for each model spacecraft was adjusted so that its laser beam hits the sensor of the other spacecraft. A control console was set up for controlling the angular velocity of the leader and its laser remotely via an IR link. Also, an IR telemetry system was setup to monitor the rotational motion of each model spacecraft.

III. Rule-Based Controls

For multiple model spacecraft, the control algorithms for the leader and followers are essentially identical. Therefore, we shall consider only a leader–follower pair in the subsequent development. The situation is analogous to a pair of ice skaters trying to spin in synchrony subject to the constraint that they can see each other only over a short time interval during each revolution. Although the skaters' corrective actions to achieve synchrony are not clearly understood, it is known that the corrective action of each skater is based solely on the visual observation of the other skater, and no quantitative information or computation of any kind is involved. This fact provides our motivation for seeking simple control laws based on the occurrence and timing of certain events to achieve synchronized rotation of the model spacecraft.

In our model spacecraft, the recognition and timing of events are achieved by using optical sensors with binary outputs. All adjustments toward synchronization are performed by the follower. By the use of the clock provided by its onboard CPU, the follower records the occurrence times of two different types of events: event A where the follower's sensor is hit by the leader's laser beam and event B where the leader's sensor is hit by the follower's laser beam.

The occurrence of event B is made known to the follower via an IR transmission from the leader. From these data, the follower obtains both its own rotation period and that of the leader, as well as the phase difference (difference between the rotation angles of the leader and follower relative to an inertial frame). When it is assumed that both the leader and follower rotate in the same direction, synchronization is attained when their rotation periods match and the phase difference is equal to some prescribed value.

In what follows, we regard the synchronization process as a chain of events of types A and B. The angular velocity synchronization corresponds to matching the difference between the occurrence times of successive events of the same type, whereas phase synchronization corresponds to making the difference between the occurrence times of successive events of different types equal to some desired value.

In rotating systems, a natural ambiguity occurs when attempting to match phase. That is, given a present event of one type, should we strive to adjust the time between it and a previous event of the other type, or wait for the next event of the other type? This ambiguity is resolved by stipulating that control action for the phase correction be taken only on the occurrence of a certain sequence of events. Because our system's configuration does not permit prediction of the system's future behavior, as in the case where the system motion can be viewed from above using an imaging device, predictive controls are ruled out. It may be argued that waiting for more events to pass before taking a more sophisticated corrective action is actually less desirable. Other than the stipulation that phase correction is activated only after the occurrence of a specific sequence of events, we strive to reduce the algorithm's complexity by taking action as soon as sufficient data become available rather than storing data for use at some opportune time.

The development of the control algorithm for this experiment is closely related to our particular experimental setup. Although our algorithm is less general, it serves as an indication of the minimum complexity that is needed to accomplish the task.

Let t_k^L be the kth time instant (according to the follower's clock) when the follower's laser beam hits the leader's sensor (occurrence time of event B) and be t_k^F the kth time instant (according to follower's clock) when the leader's laser beam hits the follower's sensor (occurrence time of event A). The rotation periods of the follower and leader are given, respectively, by

$$T_k^F = t_k^L - t_{k-1}^L, \qquad T_k^L = t_k^F - t_{k-1}^F \tag{8}$$

Synchronized rotation of the leader and follower is attained when $T_k^L = T_k^F$ and the phase difference $\phi(t_k) = \theta_L(t_k) - \theta_F(t_k)$ is equal to a prescribed value, where θ_L and θ_F are the angles that the laser beams of the leader and follower make with respect to the axis defined by the line joining the rotation centers as shown in Fig. 5a. The timing diagram and event types are shown in Fig. 5b.

When both the rotation periods of the follower and leader are available, the value of $\hat{\omega}_d$ is updated by the following rule:

$$\hat{\omega}_d\left(t_{k+1}^i\right) = \left(T_k^F / T_k^L\right)\hat{\omega}_d\left(t_k^i\right), \qquad i = L, F \tag{9}$$

where T_k^F and T_k^L are the rotation periods of the follower and leader, respectively, as defined earlier. Note that Eq. (9) applies only to the follower. Clearly, when $T_k^F = T_k^L$, then no change in $\hat{\omega}_d$ results. A low/high follower angular velocity, implying a long/short follower rotation period, results in an increase/decrease in $\hat{\omega}_d$. The foregoing rule does not depend on any knowledge of the motor power settings of the leader. Moreover, angular velocity correction takes place when a new event of either type occurs. A hit by the leader's laser beam updates the leader's period, whereas the reception of an IR message from the leader updates the follower's own period. Thus, correction of follower's angular velocity is activated twice during any rotation period. By correcting the follower's angular velocity as soon as new data become available, we avoid the ambiguity mentioned earlier

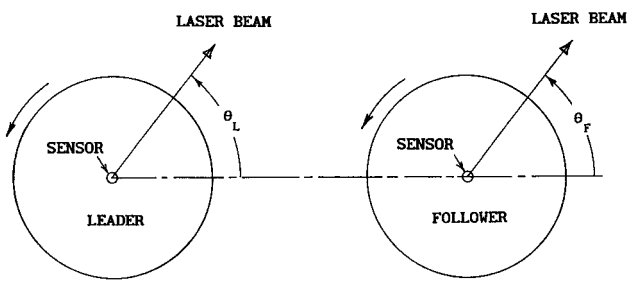

Fig. 5a Rotation angles of leader and follower.

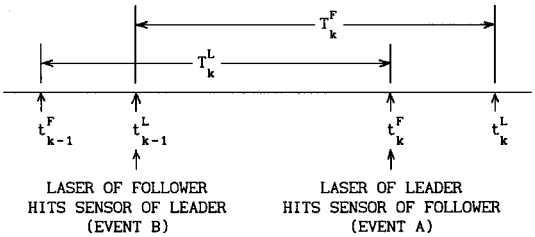

Fig. 5b Timing diagram and event types.

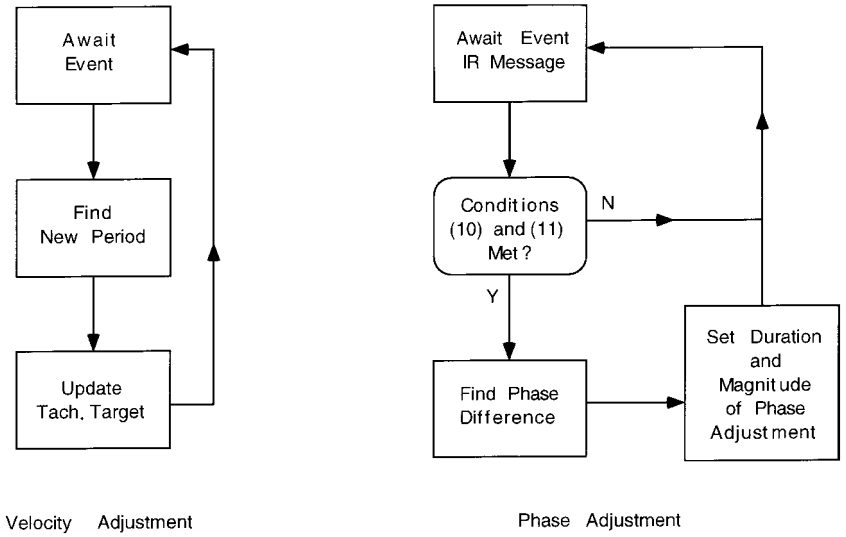

Fig. 6 Flow charts for the rule-based controls.

and the necessity of storing past data. In our experiment, all of the model spacecraft are basically identical. However, our rule is applicable also for nonidentical model spacecraft.

In phase correction, we make use of the occurrence time of either type of events based on the follower's own internal clock. To facilitate the observance of phase alignment, we set the desired phase difference to π or half of the rotation period so that exact phase alignment is indicated by the leader's and follower's laser beams rotating in synchrony, with the same heading at all times. Thus, the spots produced by the laser beams on the laboratory wall move together as the leader and follower rotate in synchrony. This choice of the desired phase difference does not require the microcontroller to handle simultaneous occurrence of events A and B, that is, the follower's sensor being hit by the leader's laser beam and the leader's sensor being hit by the follower's laser beam at the same time.

Because phase correction is effective only when the angular speeds of the leader and follower are close to each other, we activate phase correction only when

$$\left|T_k^F - T_k^L\right| \leq \eta \tag{10}$$

where η is a specified small positive number whose reciprocal value defines a phase correction region in the relative rotation-speed space. To simplify the phase-correction rules and to avoid ambiguities, we introduce, in addition to Eq. (10), a second condition on the types of present and the previous events: The present event is defined as when the follower receives an IR message from leader and the previous event as when the leader's laser beam hits follower's sensor. Thus, phase correction is activated when both conditions (10) and event types are satisfied. In stipulating event type conditions, no phase correction is made when two events of the same type occur consecutively. Moreover, the possibility of having the corrective action during one cycle being undone by that during the next cycle is avoided.

To derive a phase-correction control, we consider the phase error (expressed in units of time) as given by

$$\delta T = t_k^F + \tfrac{1}{2}T_k^L - t_k^m \tag{11}$$

where t_k^m is the time for receiving the IR message from the leader acknowledging its sensor being hit by the follower's own laser beam. Because of processing delay, t_k^m differs slightly from t_k^L, the time instant when the follower's laser beam hits the leader's sensor. The term $T_k^L/2$ is added so that the lasers of the leader and follower have the same heading when the phase error is zero. Because the follower's rotation velocity is the only physical quantity that we can directly control, zeroing the phase error must also be accomplished by manipulating its rotation speed by either momentarily speeding up or slowing down without affecting rotation speed synchronization at the end of the phase correction period. We propose to accomplish this task using the following approach.

Suppose it is necessary for the follower to reduce the phase error δT computed using Eq. (11) by speeding up the rotation. We introduce a perturbation $\delta\hat{\omega}_d$ in $\hat{\omega}_d$ over a small fraction of T_k^F, for example, δT_p, for several subsequent rotation periods so that

$$\delta\hat{\omega}_d \delta T_p = \omega^F \delta T \tag{12}$$

where ω^F is the angular velocity of follower.

We observe that, for fixed $\delta\hat{\omega}_d \delta T_p$, Eq. (12) is satisfied for small phase error δT with high rotation speed $|\omega^F|$ as well as large phase error with low rotation speed. In reality, it is difficult to make phase corrections at high rotation speeds because $\delta\hat{\omega}_d$ cannot be made large due to motor speed saturation.

Figure 6 shows the flow charts for the mentioned rotation speed and phase rule-based control algorithms. These algorithms were coded in assembly language of the Motorola 68HC11 microcontroller. Interrupts were used to check the sensors for the occurrence of events. The structure of the program consists of a main routine, which is idle until an event (either sensor hit by the leader's laser beam or the reception of an IR message from the leader) occurs. The occurrence time and type of event are recorded. These data are used to extract the rotation speed and phase information. At any instant of time, only four consecutive event occurrence times are stored in the microcontroller memory. Rotation speed control is activated after every event occurrence because each new event updates either the leader's rotation period T_L or the follower's own rotation period T_F. Phase-correction control is activated when conditions (10) and event type conditions are both satisfied. Thus, its activation is limited to at most once per revolution of the follower when its rotation speed is close to that of the leader. Finally, additional rules may be added to increase the robustness of the controls with respect to sensor data variations. For example, if the laser beam fails to activate the sensor at one or more time instants for some reason, then the estimation of the rotation period of the model spacecraft will be in error, which in turn leads to incorrect controls. This problem can be resolved by incorporating a rule that checks for sudden changes in the values of estimated rotation period and replacing the data by the previously computed good estimates.

IV. Hybrid Model

Because our experimental system is basically a hybrid continuous-time and discrete-event system, its dynamic modeling involves a mixture of differential equations and logic-based control rules driven by discrete events. In what follows, we shall show that our system with the proposed rule-based controls can be described by an unusual difference equation whose sampling time

instants are state dependent. For simplicity, we assume that the sensors have zero surface area and that they can be represented by points at the rotation centers. Let the angles θ_F and θ_L be defined in Fig. 5. Thus, the follower's laser beam hits the leader's sensor when $\theta_F = (2n+1)\pi$, $n = 0, 1, 2, \ldots$. Similarly, the laser beam of the leader hits the follower's sensor when $\theta_L = 2n\pi$, $n = 0, 1, 2, \ldots$.

Now, the equation for θ_F has the form (5), whose solution with initial condition at t_k^F and with $\hat{\omega}_d$ held constant over the sampling period is given by

$$\begin{bmatrix}\theta_F(t)\\ \dot{\theta}_F(t)\end{bmatrix} = \begin{bmatrix}1 & 1/\alpha\{1-\exp[-\alpha(t-t_k^F)]\}\\ 0 & \exp[-\alpha(t-t_k^F)]\end{bmatrix}\begin{bmatrix}\theta_F(t_k^F)\\ \dot{\theta}_F(t_k^F)\end{bmatrix} + \begin{bmatrix}1/\alpha(t-t_k^F)+(1/\alpha^2)\{\exp[-\alpha(t-t_k^F)]-1\}\\ 1/\alpha\{1-\exp[-\alpha(t-t_k^F)]\}\end{bmatrix}u(t_k^F) \tag{13}$$

where

$$\alpha = (\nu + K)[1 + (I_2/I_1)], \qquad u(t_k^F) = (K/I_1)\hat{\omega}_d(t_k^F) \tag{14}$$

The next sampling time instant t_{k+1}^F is determined by setting $\theta_F(t_{k+1}^F) = (2n+1)\pi$ for some $n = 0, 1, 2, \ldots$. Using the first equation in Eq. (13), we obtain the following transcendental equation for t_{k+1}^F:

$$\alpha[(2n+1)\pi - \theta_F(t_k^F)] = \{1-\exp[-\alpha(t_{k+1}^F - t_k^F)]\}\dot{\theta}_F(t_k^F) + (t_{k+1}^F - t_k^F + (1/\alpha)\{\exp[-\alpha(t_{k+1}^F - t_k^F)-1]\})u(t_k^F) \tag{15}$$

Evidently, t_{k+1}^F is a nonlinear function of the state $[\theta_F(t_k^F), \dot{\theta}_F(t_k^F)]$ at the kth time instant t_k^F. When t_{k+1}^F is determined, the value of $\dot{\theta}_F(t_{k+1}^F)$ is uniquely determined by the second equation in Eq. (13). If we introduce the first-order approximation for the exponential function

$$\exp[-\alpha(t_{k+1}^F - t_k^F)] \approx 1 - \alpha(t_{k+1}^F - t_k^F)$$

then Eq. (15) reduces to

$$t_{k+1}^F = t_k^F + \frac{(2n+1)\pi - \theta_F(t_k^F)}{\dot{\theta}_F(t_k^F)} \tag{16}$$

which is independent of $u(t_k^F)$. The second equation in Eq. (13) at $t = t_{k+1}^F$ reduces to

$$\dot{\theta}_F(t_{k+1}^F) = \exp\left\{-\frac{\alpha[(2n+1)\pi - \theta_F(t_k^F)]}{\dot{\theta}_F(t_k^F)}\right\}\dot{\theta}_F(t_k^F) + \frac{1}{\alpha}\left(1-\exp\left\{-\frac{\alpha[(2n+1)\pi-\theta_F(t_k^F)]}{\dot{\theta}_F(t_k^F)}\right\}\right)u(t_k^F) \tag{17}$$

If we introduce a second-order approximation for the exponential function in Eq. (17), then under the assumption that

$$u(t_k^F) > \alpha\dot{\theta}_F(t_k^F) \tag{18}$$

we have

$$t_{k+1}^F = t_k^F + \frac{1}{u(t_k^F) - \alpha\dot{\theta}_F(t_k^F)}\left(-\dot{\theta}_F(t_k^F) + \{\dot{\theta}_F^2(t_k^F) + 2[(2n+1)\pi - \theta_F(t_k^F)][u(t_k^F) - \alpha\dot{\theta}_F(t_k^F)]\}^{\frac{1}{2}}\right) \tag{19}$$

For the control rules given by Eqs. (9) and (11), the quantity $\hat{\omega}_d(t_k^F)$ in $u(t_k^F)$ is given by

$$\hat{\omega}_d(t_{k+1}^F) = \frac{t_k^L - t_{k-1}^L}{t_k^F - t_{k-1}^F}\hat{\omega}_d(t_k^F) \tag{20}$$

$$\delta\hat{\omega}_d\delta T_p = \omega^F[t_k^F + \tfrac{1}{2}(t_k^F - t_{k-1}^F) - t_k^m] \tag{21}$$

Equations (13–17) can also be used for determining the system behavior with other control rules via computer simulation. An analysis of the behavior of the solutions of this type of equations will be presented in a forthcoming paper.

V. Experimental Results

In a typical experimental run, the air-levitation system for the model spacecraft is activated. After the spacecraft have settled at their equilibrium heights, the rotation of the leader is initiated. When the initial angular velocity transient of the leader has subsided, its laser beam is turned on manually by remote control. The laser of the follower is activated when the leader's laser beam hits the sensor of the follower. Subsequently, the control for synchronized rotation takes over.

To determine the effectiveness of the control rule for rotation speed synchronization, experimental runs were made using control rule (9) only. The leader's rotation speed was set to increase at a constant rate, while the follower tries to track the leader's rotation speed. Figure 7 shows the time history for a typical run.

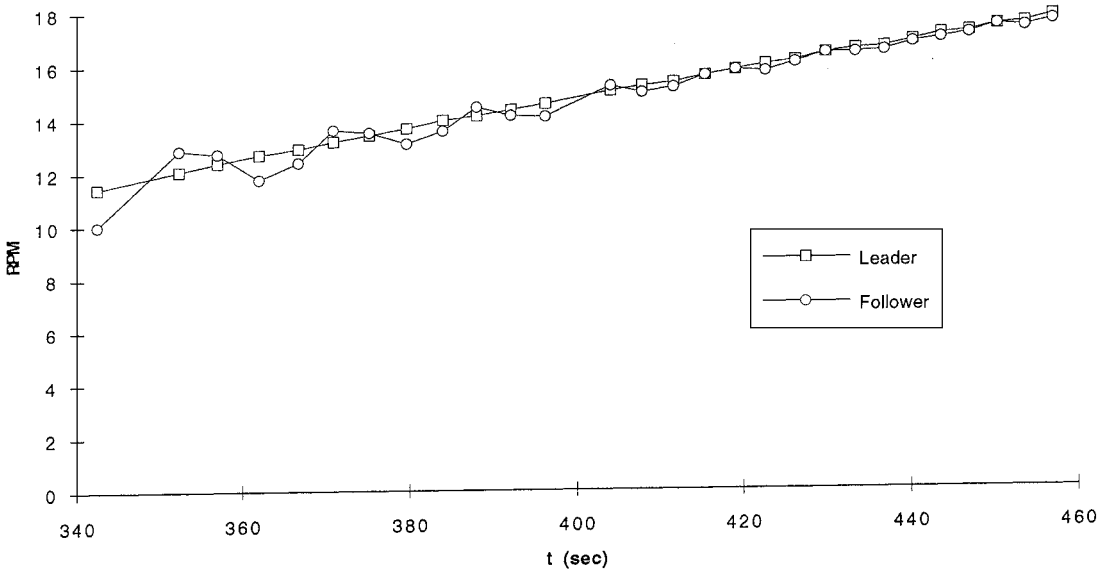

Fig. 7 Time history of rotation speeds of leader and follower with velocity control law (9) only.

The results show a small-amplitude oscillatory transient in the rotation speed tracking error during the initial 60-s period. Then the rotation speed tracking error remains within ±2% of the leader's rotation speed.

In experiments with both rotation speed and phase control algorithms activated, we had two parameters to adjust, namely, $\delta\hat{\omega}_d$ and δT_p in Eq. (12). We learned that to minimize the interaction between rotation speed and phase control algorithms, we had to keep δT_p less than about a quarter of leader's rotation period T_L while setting $\delta\hat{\omega}_d$ to the highest possible value. On the other hand, δT_p could not be set at too small a value because then the motor would have no time to react. Figure 8 shows the time history of rotation speeds and phases of the leader and follower with both speed and phase controls active and with $\delta T_p = T_L/16$. It can be seen that the phase difference after 60 s is within ±1 s. Figure 9 shows similar results for $\delta T_p = T_L/4$. In this case, it is evident that the phase control began to interact with the rotation speed control, causing larger oscillation amplitudes in the rotation speed tracking error.

To explain the observed convergence of the follower's angular velocity to that of the leader, we first determined experimentally the static relation between constant motor input voltage u and follower's rotational period T^F. From the experimental data, we obtain the following approximate expression for T^F (second) as a function of u (in units of 20 millivolts):

$$T^F = 2 + \frac{780}{u + 2u^{\frac{1}{2}} + 9} \tag{22}$$

whose graph for $0 < u \leq 200$ is shown in Fig. 10. From Eq. (22), the inverse relation is given by

$$u = [780/(T^F - 2)] - 7 - 2\{[780/(T^F - 2)] - 8\}^{\frac{1}{2}} \tag{23}$$

Because u is proportional to $\hat{\omega}_d$, we can combine control rules (9) and (23) to arrive at the following mapping Γ describing the relation between two successive rotational periods of the follower:

$$T^F_{k+1} = \Gamma\left(T^F_k\right) \tag{24}$$

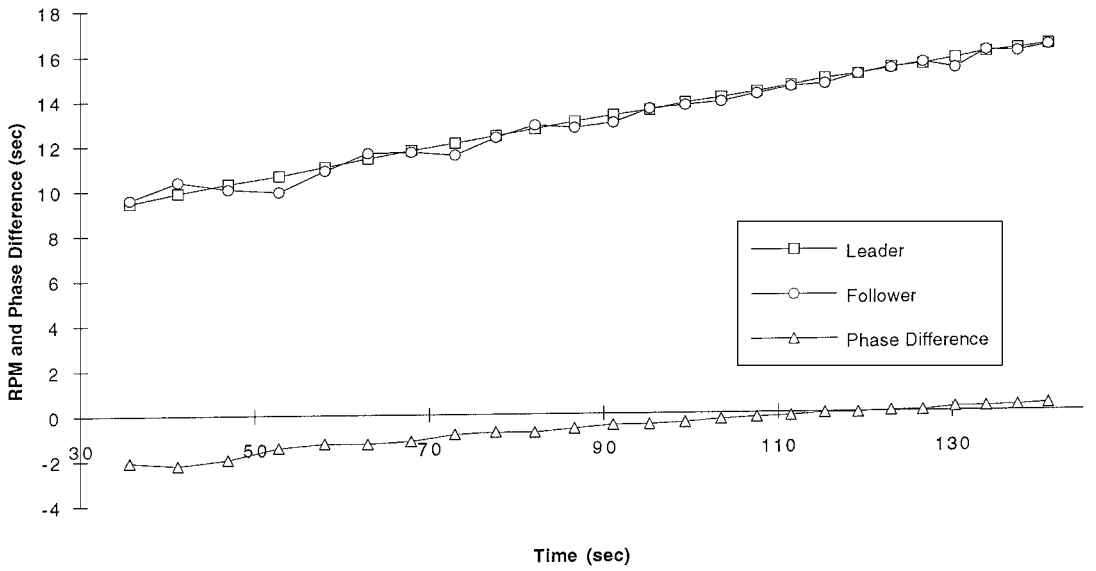

Fig. 8 Time history of rotation speeds and phases of leader and follower with both velocity and phase controls active, and with $T_p = T_L/16$.

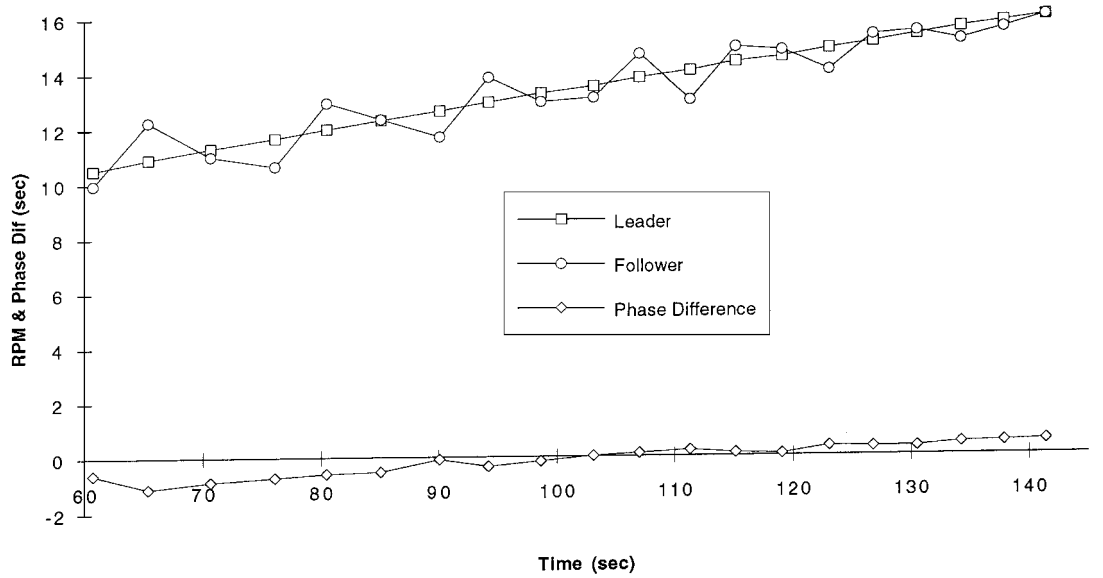

Fig. 9 Time history of rotation speeds and phases of leader and follower with both velocity and phase controls active, and with $T_p = T_L/4$.

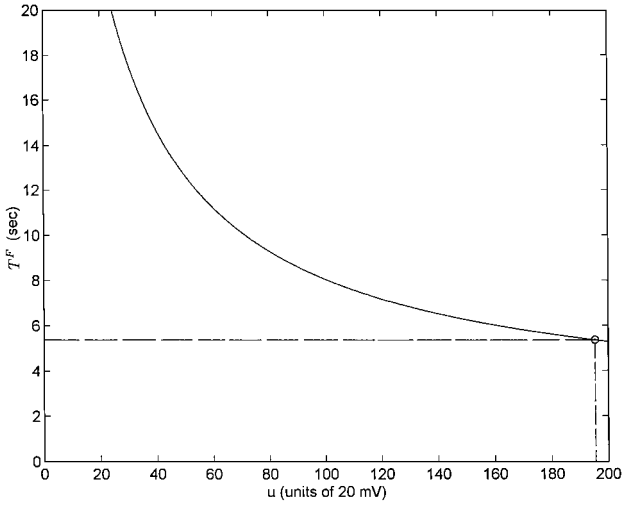

Fig. 10 Graph of T^F defined by Eq. (23); ○ indicates the maximum tachometer target voltage.

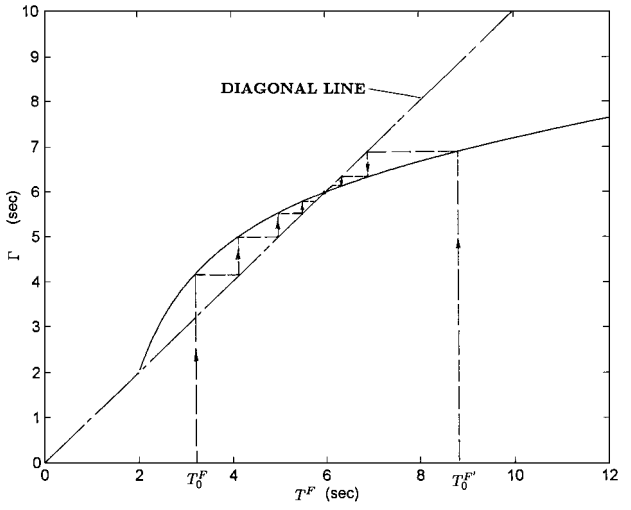

Fig. 11 Graph of Γ.

where

$$\Gamma\left(T_k^F\right) = 2 + 780\Big[8 + \Big(1 + \sqrt{T_k^F/T} \times \left\{\left[780/\left(T_k^F - 2\right) - 8\right]^{\frac{1}{2}} - 1\right\}\Big)^2\Big]^{-1} \tag{25}$$

defined for $T_k^F > 2$. The graph of Γ for $T = 6$ is shown in Fig. 11. Evidently, Γ is a contraction mapping on the interval $\mathcal{I} = \{u : 2 \le u \le 10\}$ into itself. Thus, for any $T_0^F \in \mathcal{I}$, period T_k^F converges to the stable fixed point $T^F = T$ as $k \to \infty$. This result is consistent with experimental data.

The foregoing approach to phase correction involves pulsed perturbations of the motor input power level for maintaining velocity synchronization. It was observed that these perturbations tend to induce undesirable transverse oscillatory motions of the levitated model spacecraft when the perturbation amplitude is sufficiently large. This observation led to the development of the following integrated control rule, which can be regarded as a modification of the angular velocity control rule (9) for the follower:

$$\hat{\omega}_d\left(t_{k+1}^F\right) = \frac{T_k^F}{T_k^L + \gamma\phi_k}\hat{\omega}_d\left(t_k^F\right) \tag{26}$$

where γ is a positive weighting coefficient. We repeated the experiment using the earlier integrated control rule with γ set to unity. Indeed, the experimental results show smoother control action that results in a decease in both the angular velocity and phase error at each iteration. Figure 12 shows the results of a typical experimental run. It can be seen that the follower's period tracks that of the leader after a few rotations while the phase error tends to zero in the course of time even in the presence of variations in the leader's angular velocity.

VI. Conclusions

Our experimental results showed that synchronized rotation for the model spacecraft can be achieved by using simple rule-based controls activated by the occurrence and timing of certain discrete events only. These controls do not rely on any dynamic model. The experimental results also showed that the integrated control rule given by Eq. (26) provides improved performance over that of earlier separated velocity and phase control rules given by Eqs. (9–12) and event type conditions.

Although the experiment was performed using only a pair of model spacecraft, similar experiments could be performed with more than two model spacecraft without extensive modification because the control rules for the leader and followers remain valid.

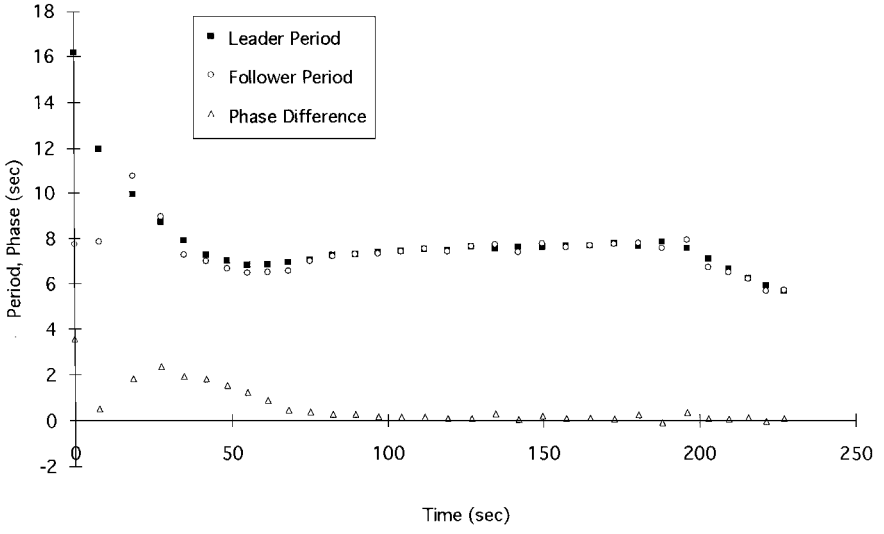

Fig. 12 Time history of rotation speeds of leader and follower with integrated control law (24).

The only necessary hardware and software modifications consist of coding and decoding the signals of the IR transceivers to permit identification of each follower and leader.

In an actual spacecraft, the laser and sensor units may be replaced, respectively, by radio-frequency beams and receivers with directional antennas with wide aperture along the axis of rotation and narrow aperture along the axes orthogonal to the rotational axis. Thus, it is unnecessary to aim the beam at the target receivers precisely.

Appendix A: Levitation System Analysis

Under the assumption that the rotational speed of the model spacecraft is small compared to the air outflow speed, the airflow is nearly axially symmetric and uniform in all radial directions. We assume also that the airflow is isothermal and laminar and that the inertial forces are negligible compared to the viscous forces in the thin air film. Thus, the steady-state air pressure $p = p(\phi)$ inside the bearing can be described by the Navier–Stokes equation satisfying the following boundary conditions:

$$p^2(\phi_0) = p_0^2, \qquad p^2(\phi_1) = p_a^2 \tag{A1}$$

where p_1 is the air pressure inside the central recess region and p_a is the ambient air pressure. The angles ϕ, ϕ_0, and ϕ_1 are defined in Fig. 2. It has been shown[10] that the solution, for the case where the sphere is concentric with the base, has the form

$$p^2(\phi) = p_a^2 + \left(p_1^2 - p_a^2\right)\frac{\ell n\{[\tan(\phi/2)]/[\tan(\phi_1/2)]\}}{\ell n\{[\tan(\phi_0/2)]/[\tan(\phi_1/2)]\}} \tag{A2}$$

Moreover, the air outflow at the rim of the spherical bearing is given by

$$q = \frac{\pi h^3}{12\mu}\left(\frac{p_a^2 - p_1^2}{p_1}\right)\left\{\ell n\left[\frac{\tan(\phi_0/2)}{\tan(\phi_1/2)}\right]\right\}^{-1} \tag{A3}$$

where μ is the viscosity of air. Equations (A2) and (A3) are valid for $p_1 \geq p_a$.

Assuming that the source pressure p_s is a positive constant and that the flow q through the orifice is in the choked regime, we have

$$q = (C_{d0}A_0C/\sqrt{T})(p_s - p_1) \tag{A4}$$

where C_{d0} and A_0 are the discharge coefficient and the area of the central orifice, respectively, T is the air temperature inside the central recess region in degrees Rankine, and C is a coefficient defined by

$$C = g\sqrt{(k/R)[2/(k+1)]^{(k+1)/(k-1)}} \tag{A5}$$

where k is the ratio of specific heats for air, g is the acceleration due to gravity, and R is the gas constant.

Using Eq. (A4) to eliminate q in Eq. (A3), and then solving for h, we obtain an explicit expression for h in terms of p_1,

$$h = \left\{\frac{12\mu C_{d0}A_0Cp_1(p_s - p_1)}{\pi\sqrt{T}\left(p_a^2 - p_1^2\right)}\ell n\left[\frac{\tan(\phi_0/2)}{\tan(\phi_1/2)}\right]\right\}^{\frac{1}{3}} \tag{A6}$$

For levitation, we balance the model spacecraft weight with the upward force f_a provided by the air bearing:

$$Mg = f_a(p_1) \overset{\text{def}}{=} 2\pi r_s^2\int_{\phi_0}^{\phi_1} p(\phi)\sin\phi\cos\phi\,\mathrm{d}\phi + \pi r_0^2 p_1 - \pi r_s^2 p_a \tag{A7}$$

where r_0 and r_s are the radii of the central recess region and the sphere, respectively, and $p(\phi)$ is given by Eq. (A2). Evidently, f_a is a nonlinear function of p_1 only. Now, given a value for Mg, the corresponding value for p_1 satisfying Eq. (A7) can be computed. Thus, the equilibrium height h can be determined from Eq. (A6) using the computed value of p_1.

Appendix B: Model Spacecraft Parameter Values

Table 1B Values of model spacecraft parameters

Parameter	Description	Value
C_{d0}	Discharge coefficient of central orifice	1.0
A_0	Area of central orifice	1.9174×10^{-4} in.^{2}
C	Coefficient defined in Eq. (2)	$0.532(^\circ\text{R})^{1/2}$/s
T	Temperature	529.67° R
M	Total mass of model spacecraft	0.0636 slug
p_s	Air source absolute pressure	94 psi
p_a	Ambient pressure	14.7 psi
r_s	Radius of spherical model spacecraft	3 in.
r_0	Radius of central recess region	0.375 in.
k	Ratio of specific heats for air	1.4
R	Gas constant	2.47×10^5 in.^{2}/(s^2) °R
μ	Absolute viscosity of air at 1 atm	1.023×10^{-6} lb/(in.s)

Acknowledgments

This work was performed under Contract 960570 with the Jet Propulsion Laboratory, California Institute of Technology, Pasadena, California. The authors thank the referees for their helpful comments and suggestions.

References

[1]Stachnik, R., Melroy, R., and Arnold, D., "Multiple Spacecraft Michelson Stellar Interferometry," *Proceedings of the SPIE Instrumentation in Astronomy*, Vol. 5, No. 445, 1984, pp. 358–369.

[2]De Cue, A. B., "Multiple Spacecraft Optical Interferometry, Preliminary Feasibility Assessment," Jet Propulsion Lab., Technical Internal Rept. D-8811, California Inst. of Technology, Pasadena, CA, Aug. 1991.

[3]Wang, P. K. C., and Hadaegh, F. Y., "Coordination and Control of Multiple Microspacecraft Moving in Formation," *Journal of Astronautical Sciences*, Vol. 44, No. 3, 1996, pp. 315–355.

[4]Beard, R. W., McLain, T. W., and Hadaegh, F. Y., "Fuel Equalized Retargeting for Separated Spacecraft Interferometry," *Proceedings of the American Automatic Control Conference*, IEEE Publications, Piscataway, NJ, 1998, pp. 1580–1584.

[5]Wang, P. K. C., and Hadaegh, F. Y., "Optimal Formation Reconfiguration for Multiple Spacecraft," *Proceeding of the AIAA Guidance, Navigation, and Control Conference*, AIAA, Reston, VA, 1998, pp. 686–696.

[6]Wang, P. K. C., Hadaegh, F. Y., and Lau, K., "Synchronized Formation Rotation and Attitude Control of Multiple Free-Flying Spacecraft," *Journal of Guidance, Control, and Dynamics*, Vol. 22, No. 1, 1999, pp. 28–35.

[7]Ullman, M. A., "Experiments in Autonomous Navigation and Control of Multi-Manipulator Free Flying Space Robots," Ph.D. Dissertation, Dept. of Aeronautics and Astronautics, Stanford Univ., Stanford, CA, March 1993.

[8]Zimmerman, K. R., and Cannon, R. H., Jr., "Experimental Demonstration of GPS for Rendez-vous Between Two Prototype Space Vehicles," *Proceedings of the Institute of Navigation GPS-95*, Inst. of Navigation, Alexandria, VA, Sept. 1995.

[9]Wang, P. K. C., Yee, J., Hadaegh, F. Y., and Lau, K., "Experimental Study of Multiple Air-Levitated Vehicles Moving in Formation," *Journal of Robotic Systems*, Vol. 15, No. 10, 1998, pp. 559–580.

[10]Laub, J. H., and Norton, R. H., Jr., "Externally Pressurized Spherical Gas Bearings," *American Society of Lubrication Engineers*, Vol. 4, 1961, pp. 172–180.